Two-dimensional pulsed-plasma simulation of a chlorine discharge

Badri Ramamurthi and Demetre J. Economou[a)]
Plasma Processing Laboratory, Department of Chemical Engineering, University of Houston, Houston, Texas 77204-4004

(Received 6 August 2001; accepted 17 December 2001)

A two-dimensional (r,z) continuum model was developed to study the spatiotemporal dynamics of a pulsed power (square-wave modulated) chlorine discharge sustained in an inductively coupled plasma (ICP) reactor with a planar coil. The self-consistent model included Maxwell's equations for the power deposition profiles coupled to the electron energy equation and the species mass balances. Simulation results showed separation of the plasma into an electronegative core and an electropositive edge during the active glow (power on) and the formation of an ion–ion plasma $\sim 15\ \mu$s into the afterglow (power off). During the early active glow, the negative ion flux was convection dominated near the quartz window of the ICP reactor due to the formation of large electrostatic fields, leading to a self-sharpening front propagating into the plasma. The negative ion density profiles were found to have a strong spatial dependence underlying the importance of spatial resolution in negative ion density measurements. The time dependent ion and radical flux uniformity was also studied. Simulation results were compared with experimental data and reasonable agreement was observed. © *2002 American Vacuum Society.* [DOI: 10.1116/1.1450581]

I. INTRODUCTION

Low pressure (<100 mTorr) glow discharge plasmas are used extensively in microelectronics for etching and deposition of thin films.[1] Pulsed power operation (e.g., square-wave modulated power input to the plasma) may offer potential improvements of reactor performance. For example, etch or deposition rate and uniformity may be improved,[2,3] particulate density may be reduced,[4] or anomalous etch profiles may be suppressed.[5]

Pulsed power electronegative discharges are of particular practical importance since the vast majority of gases used for plasma processing are electronegative. In such plasmas, negative ions replace electrons as the dominant negative-charge carrier sometime in the afterglow, provided the afterglow phase is long enough. A positive ion/negative ion (ion–ion) plasma is then formed and negative ions can escape the discharge.[6–8] Since the temperature and mass of negative ions are comparable to those of positive ions, the flux of positive and negative ions will be equally anisotropic, potentially reducing differential charging on the walls of microscopic features on the wafer surface. For instance, Ahn *et al.*[5] applied a low frequency bias (600 kHz) in the afterglow of a pulsed chlorine discharge to achieve significant reduction in charging damage (notching) compared to a continuous wave (cw) plasma. This was attributed to alternate irradiation[9] of positive ions and negative ions leading to reduced surface charging.

In order to improve understanding of pulsed plasmas in electronegative gases, and elucidate how these plasmas may affect processing, it is worthwhile to model the spatiotemporal plasma evolution in realistic reactor geometries. Existing pulsed plasma models and simulations are limited to well mixed (0D)[10,11] and one-dimensional (1D) works.[6,12] In this article, a two-dimensional (2D) self-consistent continuum (fluid) model was developed to simulate the spatiotemporal evolution of an inductively coupled pulsed chlorine discharge in a GEC reference cell.[13] The power deposition was calculated self-consistently as opposed to a uniform power deposition used in the 1D work.[6] In previous studies, a modular approach was used to simulate cw plasma operation, in which only the ''steady state'' was of interest.[14] In contrast, in the present work, the coupled equations for plasma power deposition, electron temperature, and charged and neutral species densities were solved simultaneously to capture the time-dependent discharge evolution.

II. MODEL FORMULATION

Figure 1 shows a schematic of an inductively coupled GEC reference cell, which can generate a high density plasma inside a chamber bounded by a quartz window and metal walls. The plasma is driven by a 5-turn planar coil powered at 13.56 MHz. The rf current in the coil produces a time-varying magnetic field, which in turn induces an azimuthal electric field heating the plasma electrons. The model consisted of the electromagnetic equation for the self-consistent azimuthal electric field powering the plasma, an equation for the electron temperature (assuming Maxwellian electrons), and mass continuity equations for the charged (Cl^+, Cl_2^+ and Cl^-) and neutral (Cl) species. The model equations are described in the following sections. Details of the formulation may be found in published works.[15,16] The electron density was calculated by charge neutrality. This implies that the thin sheath near the reactor walls was not included in the simulation. Since the sheath is only hundreds of microns thick in the high density plasma, boundary conditions were effectively applied at the geometric location of the walls. The reaction set for chlorine (Table I) was the same as before,[16] except that the charge exchange Cl^+

a)Electronic mail: economou@uh.edu

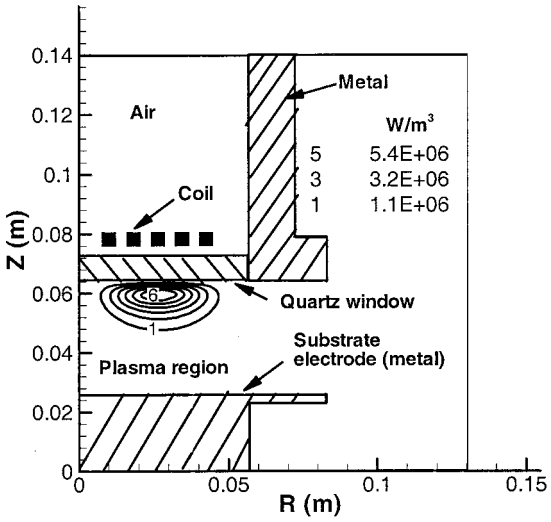

FIG. 1. Schematic of the GEC-ICP reactor. The quasi-steady state power deposition profile is also shown.

$+Cl_2 \rightarrow Cl + Cl_2^+$ reaction[17] was also incorporated in the chemistry set. The assumptions of the model were as follows.

(1) The fluid approximation was used since $\lambda/L = 0.1$, where λ is the mean-free path ($\sim$0.5 cm) and L is a characteristic dimension of the reactor ($\sim$5 cm).

(2) The species densities, electron temperature, and induced electric field were assumed to be azimuthally symmetric, and magnetic field[18] effects were not considered.

(3) The charged particle flux was described by the drift-diffusion approximation (spatial inertia was neglected in the momentum equations) since the pressure was >10 mTorr.

(4) The electron energy distribution function (EEDF) was assumed Maxwellian and an equation for the electron temperature was solved.

(5) Particle mobilities and diffusivities were assumed constant for a given pressure.

(6) Electron heating was assumed to be collisional (ohmic). Noncollisional heating[19] can become important at low pressures when $v_T/\delta > \omega,\ \nu_m$, where the symbols stand for electron thermal velocity, skin depth, applied field frequency, and electron collision frequency for momentum transfer, respectively.

(7) Ions and neutrals were assumed to be at 300 K. Hence a heavy species energy equation was not solved.

A. Electromagnetics

Under the assumption of azimuthally symmetric electric field, with a time harmonic dependence of the form $e^{-j\omega t}$, Maxwell's equations can be reduced to a single scalar equation in E_θ. In cylindrical coordinates,

$$\frac{1}{r}\frac{\partial}{\partial r}\left(r\frac{\partial E_\theta}{\partial r}\right)+\frac{\partial^2 E_\theta}{\partial {z}^2}-\frac{E_\theta}{r^2}+\frac{\omega^2}{c^2}K_c E_\theta = -j\omega\mu_0 J_\theta^i, \quad (1)$$

where ω is the frequency of the coil current, μ_0 is the vacuum permeability, K_c is the complex permittivity of the plasma (which depends on the electron density), J_θ^i is the impressed current density in the coils, and c is the speed of

TABLE I. Important reactions in a low pressure chlorine discharge.

No.	Process	Reaction	H_j (eV)
Electron impact reactions			
R1	molecular ionization	$e+Cl_2 \rightarrow Cl_2^+ + 2e$	11.47
R2	atomic ionization	$e+Cl \rightarrow Cl^+ + 2e$	12.99
R3	dissociative attachment	$e+Cl_2 \rightarrow Cl^- + Cl$	
R4	electron–ion neutralization	$e+Cl_2^+ \rightarrow 2Cl$	
R5	electron detachment	$e+Cl^- \rightarrow Cl+2e$	3.61
R6	dissociative excitation	$e+Cl_2 \rightarrow 2Cl+e$	3.12
Molecular excitations		$e+Cl_2 \rightarrow Cl_2^* + 2e$	
R7	$B^3\Pi$		2.49
R8	$2^1\Pi,\ 2^1\Sigma$		9.25
Atomic excitations		$e+Cl \rightarrow Cl^* + 2e$	
R9	$4s$		8.90
R10	$4p$		10.40
R11	$3d$		10.90
R12	$5p$		11.80
R13	$4d$		12.00
R14	$5d$		12.40
Other reactions			
R15	ion–ion recombination	$Cl_2^+ + Cl^- \rightarrow Cl_2 + Cl$	
R16	wall recombination	$2Cl + wall \rightarrow Cl_2 + wall$	
R17	charge exchange	$Cl^+ + Cl_2 \rightarrow Cl_2^+ + Cl$	

light. At low frequencies, the current in the coil is nearly constant and the above equation may be solved for constant J_θ to determine E_θ in the reactor. However, at higher frequencies, a circuit model is required to account for capacitive coupling between the coil and the plasma (the current changes from loop to loop).[20] In the present work, the procedure of Jeager *et al.*[20] as adopted by Midha and Economou[21] was used to calculate the power deposition. The power deposited in the plasma was computed by

$$P = \tfrac{1}{2}\mathrm{Re}(\sigma_p)|E_\theta|^2, \tag{2}$$

where $\mathrm{Re}(\sigma_p)$ is the real part of σ_p, the complex plasma conductivity. Equation (2) assumes that the power deposited in the plasma is due to ohmic heating.[19] The conductivity was obtained from the following relations:

$$K_c = 1 - \frac{\omega_{\mathrm{pe}}^2}{\omega^2\left(1 + \frac{j\nu_m}{\omega}\right)}, \tag{3}$$

$$\sigma_p = -j\omega\varepsilon_0(K_c - 1), \tag{4}$$

$$\omega_{\mathrm{pe}}^2 = n_e e^2/m\varepsilon_0, \tag{5}$$

where ω_{pe} is the electron plasma frequency and ν_m is the electron collision frequency for momentum transfer.

In reality, during the active glow fraction of the cycle, power is initially coupled to the plasma through capacitive coupling. After the electron density exceeds a threshold value, power is then coupled in the inductive mode. The present simulation does not account for capacitive coupling. In order to emulate reality with the present model, the power was actually ramped linearly from zero to the full power level during the first 5 μs of the ''power on'' fraction of the cycle. This approach should only affect results during the first several μs of the pulse. This was indeed verified by simulations using different ramp times. The main effect was on the electron temperature spike (not the steady state value of T_e, see Fig. 2). Species densities are slower to respond and are not affected appreciably.

B. Ion transport and reaction

With the drift-diffusion flux approximation for the charged species, the continuity equation for the ions (Cl_2^+, Cl^+, Cl^-) is of the form,

$$\frac{\partial n_i}{\partial t} = -\nabla\cdot(z_i\mu_i n_i \mathbf{E}_{\mathrm{sc}} - D_i\nabla n_i) + \sum_j R_{ji}, \tag{6}$$

where n_i, z_i, D_i, and μ_i are the density, charge number, diffusivity, and mobility, respectively, of species i. $\mathbf{E}_{\mathrm{sc}}$ is the electrostatic (space charge) field having two components (E_r and E_z). The summation on the right-hand side represents reactions that produce or destroy the respective species.

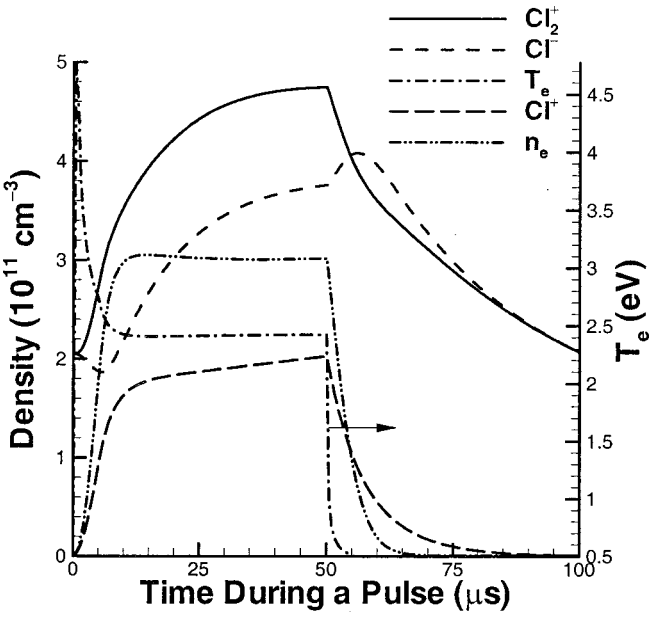

FIG. 2. Ion densities and electron temperature evolution at the center of the reactor (base case conditions).

Boundary conditions employed were $J_i = 0$ on the symmetry axis, where J_i is the ion flux, and $n_i \approx 0$ on the rest of the boundary. The electrostatic field was derived assuming no net current in the plasma. Equating the positive and negative charge fluxes, one obtains

$$\mathbf{E}_{\mathrm{sc}} = \frac{D_{p_1}\nabla n_{p_1} + D_{p_2}\nabla n_{p_2} - D_n\nabla n_n - D_e\nabla n_e}{\mu_{p_1} n_{p_1} + \mu_{p_2} n_{p_2} + \mu_n n_n + \mu_e n_e}. \tag{7}$$

The electron density n_e was obtained from quasi-neutrality as $n_e = n_{p_1} + n_{p_2} - n_n$ where n_{p_1}, n_{p_2}, and n_n are Cl^+, Cl_2^+, and Cl^- densities, respectively.

C. Electron temperature

The electron energy equation reads

$$\frac{\partial}{\partial t}\left(\frac{3}{2}n_e T_e\right) = -\nabla\cdot\mathbf{q}_e + P - \sum_j R_{je}\Delta H_j, \tag{8}$$

$$\mathbf{q}_e = -K_e\nabla T_e + \tfrac{5}{2}\mathbf{J}_e T_e, \tag{9}$$

where $\mathbf{q}_e$ is the electron energy flux, K_e is the electron thermal conductivity, and J_e is the electron flux. The second term on the right hand side (rhs) represents the power deposited into the electrons due to ohmic heating [Eq. (2)]. The third term on the rhs represents the electron energy lost due to elastic and inelastic collisions. The electron density decays quite rapidly in the afterglow. Therefore a finite value of n_e was fixed in order to prevent the energy balance equation from becoming singular.[6,11] The boundary conditions were $q_e = 0$ at the centerline and $q_e = \frac{5}{2}\mathbf{J}_e T_e$ on walls. Since the

time scale for electron temperature evolution is the smallest in the system ($\sim 0.1\ \mu s$), the temperature reaches a periodic steady state most rapidly.

D. Neutral transport and reaction

The Cl atom density was computed using Eq. (10) below, assuming that transport is diffusion dominated,

$$\frac{\partial n_{\mathrm{Cl}}}{\partial t} = -\nabla \cdot (-D_{\mathrm{Cl}} \nabla n_{\mathrm{Cl}}) + \sum_j R_{j\mathrm{Cl}} - \frac{n_{\mathrm{Cl}}}{\tau_{\mathrm{res}}}, \tag{10}$$

where $R_{j\mathrm{Cl}}$ represents reactions that produce or consume Cl atoms. The boundary conditions were symmetry on axis and $-D_{\mathrm{Cl}} \nabla n_{\mathrm{Cl}} = [\gamma/2(2-\gamma)]\, n_{\mathrm{Cl}} v_{\mathrm{Cl}} - J_{\mathrm{Cl}^+}$ on walls, where γ is the recombination probability of Cl atoms on the walls ($=0.1$), v_{cl} is their thermal velocity, and J_{Cl^+} is the flux of Cl^+ ions on the walls. The Cl_2 density was obtained from n_{Cl} as $n_{\mathrm{Cl}_2} = n_g - n_{\mathrm{Cl}}$ where n_g is the total neutral density. The latter was found assuming a uniform pressure and gas temperature of 300 K. The last term in Eq. (10) accounts for convective flow losses of Cl atoms through the residence time τ_{res} ($=3.8$ ms). The response time scale for neutral species is the largest in the system (~ 1 ms). Therefore integration in time had to be performed over ten to hundreds of cycles to attain a periodic steady state.

III. METHOD OF SOLUTION

The set of nonlinear coupled PDEs for T_e and species transport [Eqs. (6)–(10)] was spatially discretized using a streamline upwind Petrov–Galerkin (SUPG) method[22] to yield a system of equations of the form

$$A(\mathbf{u})\dot{\mathbf{u}} = K(\mathbf{u})\mathbf{u} + F(\mathbf{u}), \tag{11}$$

where $\mathbf{u}$ represents the solution vector, $\dot{\mathbf{u}}$ is the time derivative of $\mathbf{u}$, and A and K are banded nonlinear mass and stiffness matrices, respectively. F is a nonlinear source vector. SUPG is better suited than the traditional Galerkin finite element method for capturing sharp gradients. The resulting set of implicit ordinary differential equations in Eq. (11) was integrated in time using backward difference formulas[23] until a periodic steady state was obtained. At each time step, the equation for the azimuthal electric field [Eq. (1)] was solved using the Galerkin finite element method and a direct band solver. The convergence criterion was set by evaluating the L^2 norm of the solution normalized with respect to the average, i.e.,

TABLE II. Base case parameter values.

Pressure	20 mTorr
Peak power	320 W
Pulse frequency	10 kHz
Duty ratio	0.5
Cl wall recombination probability	0.1
Ion temperature	300 K
Gas temperature	300 K

$$\varepsilon_j = \frac{1}{V^{1/2}} \left[\int_\Omega \left\{ \left(\frac{u_j}{\langle u_j \rangle} \right)_{(i+1)T_p} - \left(\frac{u_j}{\langle u_j \rangle} \right)_{iT_p} \right\}^2 d\Omega \right]^{1/2}, \tag{12}$$

where ε_j, u_j, and $\langle u_j \rangle$ are the tolerance parameter, dependent variable, and its average, respectively, over the domain of interest Ω. V is the plasma volume, T_p is the pulse width of the power modulation cycle, and i is the cycle number ($i=1,2,3,...$). The convergence criterion was tested at the end of each cycle; integration was terminated when the evaluated tolerance was less than a user-specified value (0.5%) for all species and electron temperature. As expected, the Cl and Cl^- densities were the slowest to converge.

IV. RESULTS AND DISCUSSION

A chlorine discharge was simulated in an inductively coupled GEC reference cell under the base case parameters shown in Table II. The mobilities of the ionic species and the Cl atom diffusivity are shown in Table III.[16] Ionic diffusivities were computed using the Einstein relation $D = \mu kT/e$, where T is temperature. Power to the plasma was square-wave modulated with the power at the peak value for the first 50 μs of the pulse (power on) followed by zero power (power off) for the remaining 50 μs (pulse period 100 μs, duty ratio of 0.5). The ''power on'' and ''power off'' phases of the cycle will be referred to as ''active glow'' and ''afterglow,'' respectively. Simulations were also performed for duty ratios of 0.3 and 0.7 and a peak power of 220 W in order to study the variation of electron density and compare simulation results with experimental data.[24] All results shown below are for the periodic steady state at the base case parameters (Table II), unless noted otherwise. In the discussion below, the discharge electronegativity was defined as the ratio of negative ion to electron density. Also discharge ''core'' and ''edge'' refer to the core and edge regions of the space in-between the parallel plates, while ''outer region'' refers to the cylindrical space surrounding the parallel plates, $8.3 < R < 13$ cm (Fig. 1).

TABLE III. Ionic mobilities and Cl atom diffusivity (N is the neutral gas density).

Name	Symbol	Value	Reference
Cl_2^+ mobility	$N\mu_{Cl_2^+}$ ($\mathrm{cm}^{-1}\,\mathrm{V}^{-1}\,\mathrm{s}^{-1}$)	5.62×10^{19}	16
Cl^+ mobility	$N\mu_{\mathrm{Cl}^+}$ ($\mathrm{cm}^{-1}\,\mathrm{V}^{-1}\,\mathrm{s}^{-1}$)	6.48×10^{19}	16
Cl^- mobility	$N\mu_-$ ($\mathrm{cm}^{-1}\,\mathrm{V}^{-1}\,\mathrm{s}^{-1}$)	6.48×10^{19}	16
Cl diffusivity	ND_{Cl} ($\mathrm{cm}^{-1}\,\mathrm{s}^{-1}$)	6.21×10^{18}	16

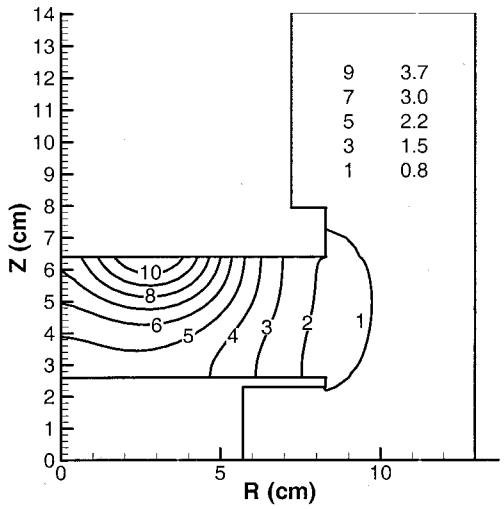

FIG. 3. Quasi-steady state (at 20 μs) electron temperature (eV) profile (base case conditions, Table II).

The quasi-steady state power deposition profile (in W/cm^3) is shown in Fig. 1. Power is deposited directly under the coil in a toroidal pattern, with a typical skin depth of $\sim$1 cm. The max power density is $\sim$7 W/cm^3 for a total power deposition of 320 W.

The time evolution of electron temperature, electron density, and ion density at the center of the discharge ($R=0$ and $z=4.5$ cm) is shown in Fig. 2. The electron temperature is controlled by a balance between electron production, mainly by ionization of atomic and molecular chlorine (reactions R1 and R2 in Table I), and loss by attachment (R3) and diffusion to the walls. Since the electron density is very low at the beginning of the active glow, the electron temperature goes through a spike before relaxing to a quasi-steady value after $\sim$10 μs. Such temperature spikes have been observed experimentally.[5,25] The electron temperature is seen to decrease rapidly in the early afterglow mainly due to inelastic losses with neutrals. The electron and ion densities all rise monotonically during the active glow. The Cl^+ density is lower when compared to Cl_2^+, in part due to charge exchange with molecular chlorine (reaction R17, Table I). This reaction is responsible for the almost complete disappearance of Cl^+ late in the afterglow. The electrons disappear $\sim$15 μs into the afterglow leaving behind an ion–ion plasma[6–8] eventually consisting of Cl_2^+ and Cl^- ions.[9]

The electron temperature distribution during the quasi steady state (Fig. 3) is highest ($\sim$4 eV) near the maximum of power deposition. Electrons cool substantially in the outer region of the reactor ($8<R<13$ cm). Despite the fact that power is deposited in a relatively small toroidal zone (Fig. 1), electrons are quite warm even far from the quartz window

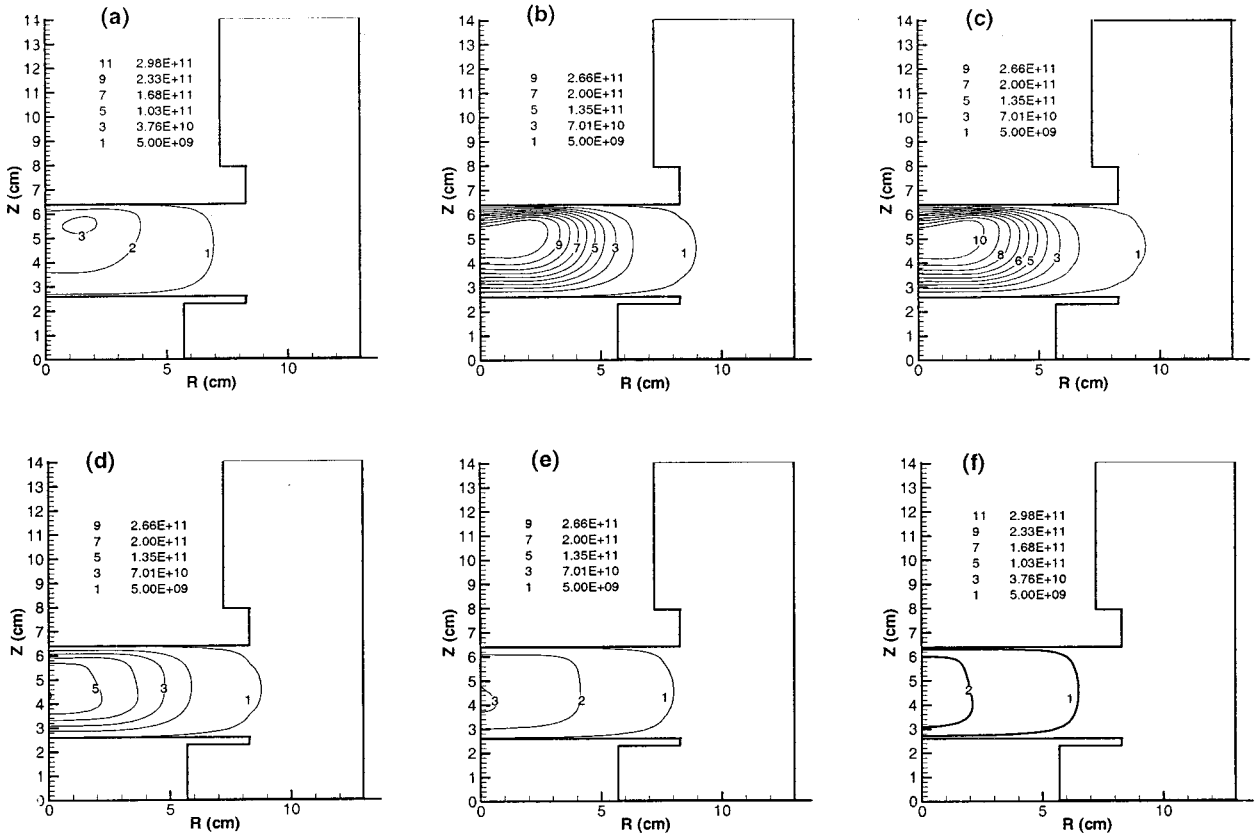

FIG. 4. Electron density (cm^{-3}) evolution at (a) 2 μs, (b) 10 μs, (c) 50 μs, (d) 53 μs, (e) 56 μs, and (f) 60 μs during a pulse (base case conditions, Table II).

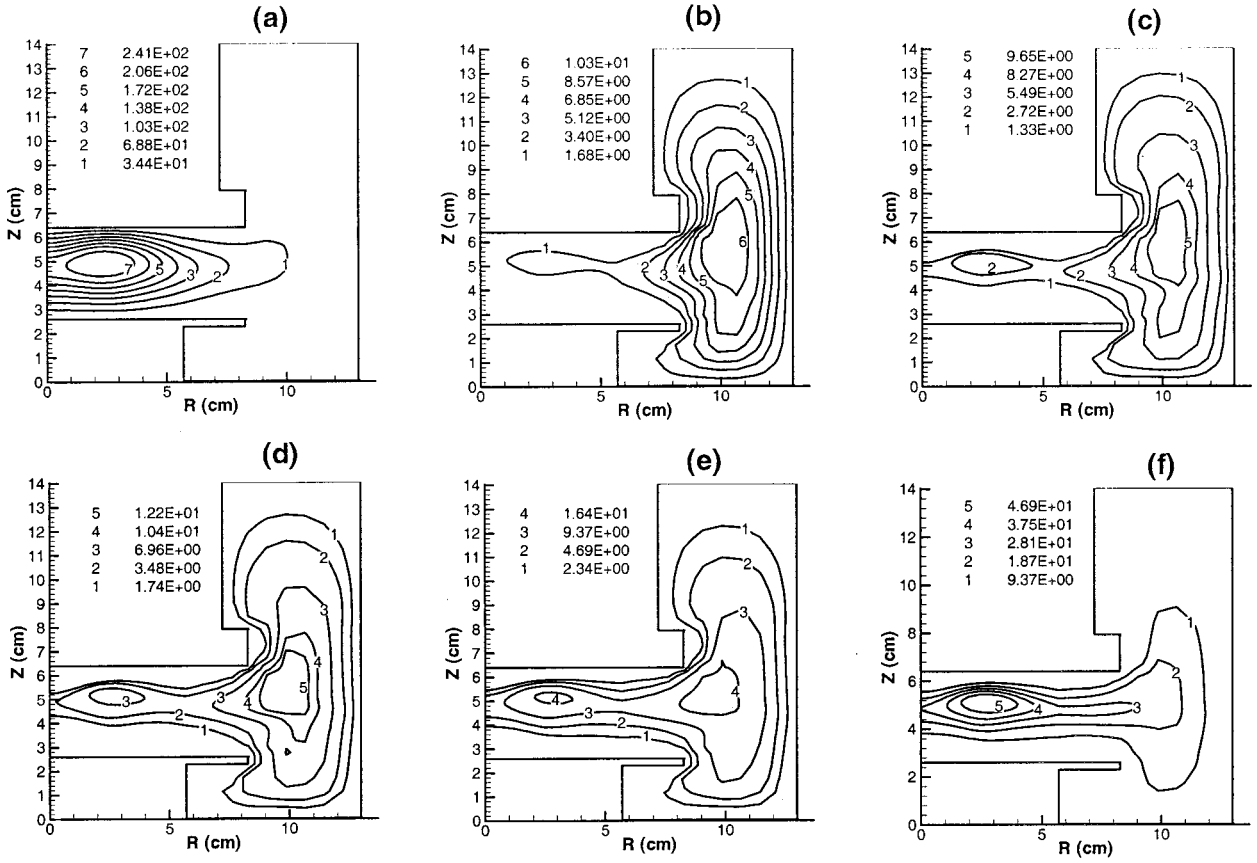

FIG. 5. Electronegativity (ratio of negative ion to electron densities) evolution at (a) 0 μs, (b) 10 μs, (c) 50 μs, (d) 53 μs, (e) 56 μs, and (f) 60 μs during a pulse (base case conditions, Table II).

(e.g., near the substrate electrode) due to the high thermal conductivity of the electron gas. Lower pressures would lead to higher electron temperatures and a more uniform temperature distribution.

The space-time evolution of electron density is shown in Fig. 4 for times of 2, 10, 50, 53, 56, and 60 μs. In the initial active glow (at time 0^+, not shown), there are only relatively few electrons to absorb power; hence most of the power is reflected. As the ionization rate increases due to a steep rise in electron temperature (Fig. 2), more electrons become available to absorb power and cause further ionization. Thus the electron density increases [Figs. 4(a) and 4(b)]. Initially [Fig. 4(a)], the electron density gradient is quite low. This is due to the high values of electronegativity [Fig. 5(a)], which lead to near neutralization of the space-charge field and thus enhanced diffusion of electrons (approaching free electron diffusion at very high electronegativities). Higher electron diffusivity leads to a smoother electron density profile. After $\sim$10 μs in the active glow [Fig. 4(b)], the electron density profile reaches a quasi-steady state. The profile remains essentially unchanged during the rest of the active glow [Fig. 4(c)], showing two distinct regions. The (inner) core of the discharge, where negative ions exist (electronegative core) and the electron density gradients are smaller, and the (outer) edge where the negative ion density is very small (electropositive edge) and the electron density gradients are larger. This stratification is also seen in the negative ion density profiles of Fig. 6(d). The drop in electronegativity later in the active glow [Figs. 5(b) and 5(c)] is attributed to the continuing build up of electron density (Fig. 2).

Figures 4(d)–4(f) show the electron density profiles in the early afterglow. The corresponding electronegativities are shown in Figs. 5(d)–5(f). Once the power is turned off, electron production by ionization quenches since the electron temperature plummets within a few μs. Electrons are lost mainly due to attachment (the attachment rate coefficient rises by an order of magnitude as electrons cool in the afterglow[11]) and diffusion to the walls. Thus the electron density drops quickly and the electronegativity rises both in the discharge core and the edge. As electrons disappear within $\sim$15 μs into the afterglow, the electrostatic fields disintegrate, an ion–ion plasma forms, and negative ions start to diffuse towards the edge [see also Fig. 6(f)]. It should be noted that there are two distinct peaks in the electronegativity profile during the late active glow and the early afterglow [Figs. 5(b)–5(e)]. The peak in the discharge core occurs due to the large number of negative ions there, while the peak in the outer region occurs due to the presence of very few electrons there.

The Cl^- density profile evolution is shown in Figs. 6(a)–6(f). At the start of a pulse, negative ions are present in the periphery due to diffusion during the afterglow of the previ-

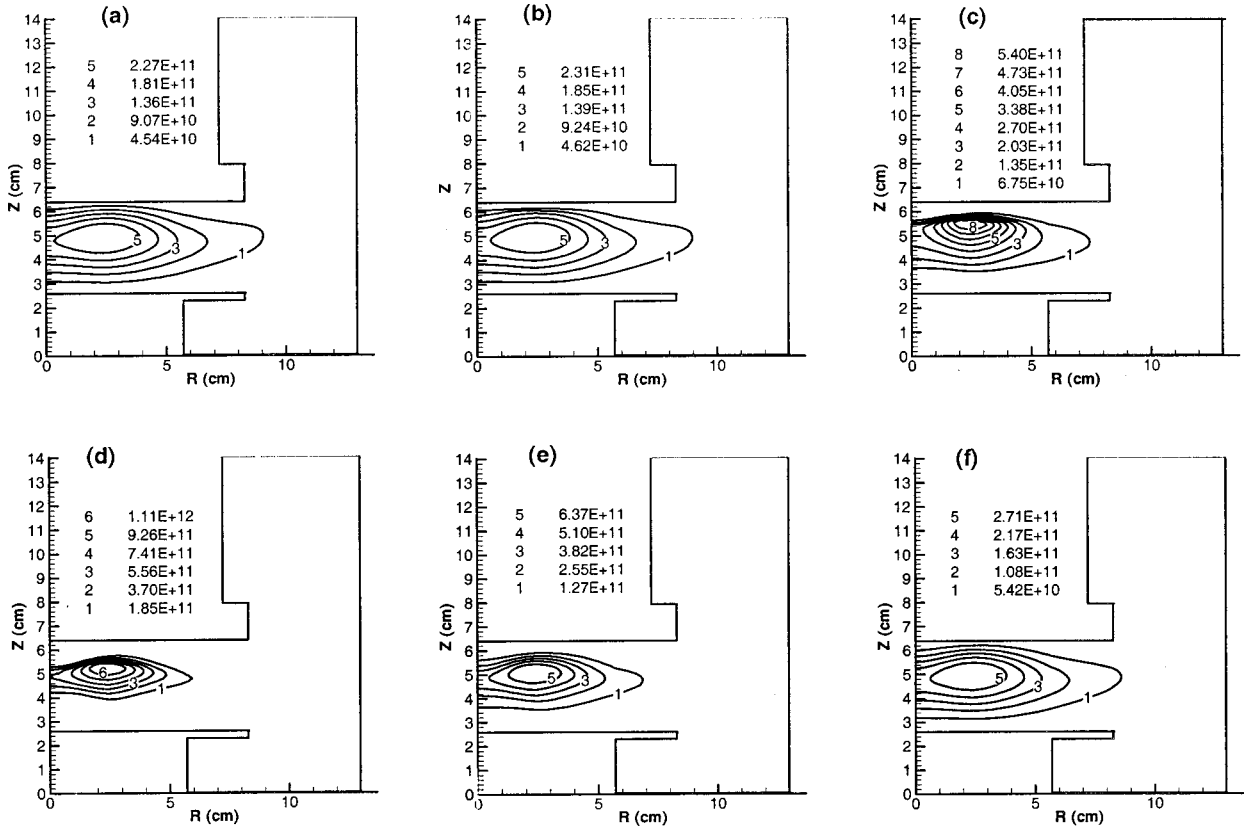

FIG. 6. Cl^- density (cm^{-3}) evolution at (a) 0 μs, (b) 1 μs, (c) 5 μs, (d) 50 μs, (e) 60 μs, and (f) 90 μs during a pulse (base case conditions, Table II).

ous pulse. As the electron temperature and electron density start to increase, the ambipolar electric field [Eq. (7)] also increases, causing negative ions to be squeezed into the plasma [Figs. 6(c) and 6(d)]. The squeezing of negative ions is stronger near the quartz window since the electron temperature is larger in that region [Fig. 3, see also Fig. 9(a) below]. Since there is negligible flux of negative ions at the wall during the active glow, the quasi-steady state of negative ion profile [Fig. 6(d)] is sustained by a balance between production processes such as attachment, and destruction processes such as detachment and ion–ion recombination. Later in the afterglow, negative ions start diffusing back towards the walls as the electric field diminishes. Their diffusion is almost free (almost no electric field) after the ion–ion plasma forms.

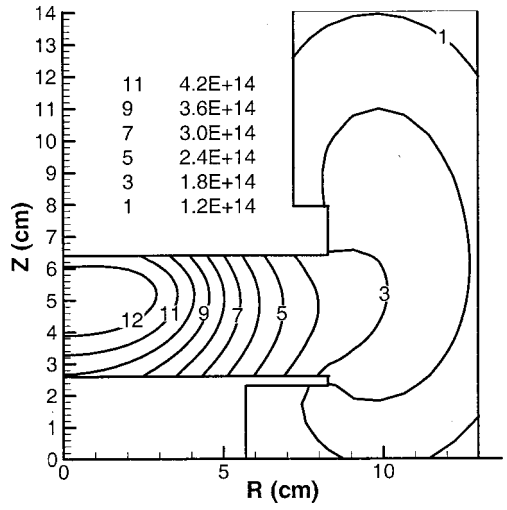

FIG. 7. Quasi-steady state Cl-atom density (cm^{-3}) profile (base case conditions, Table II).

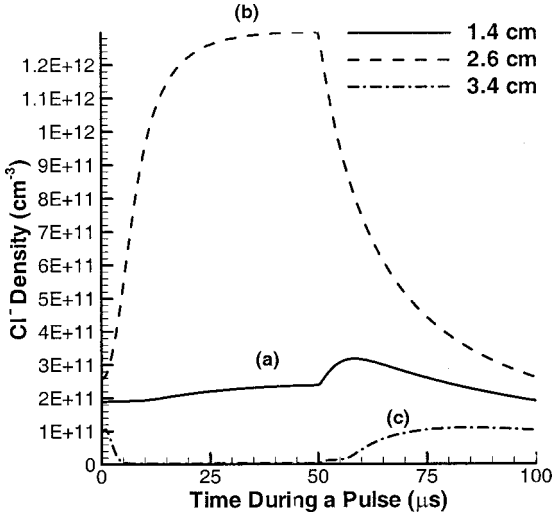

FIG. 8. Cl^- density (cm^{-3}) evolution at a radius of 2.4 cm for three axial locations measured from the substrate electrode (base case conditions, Table II).

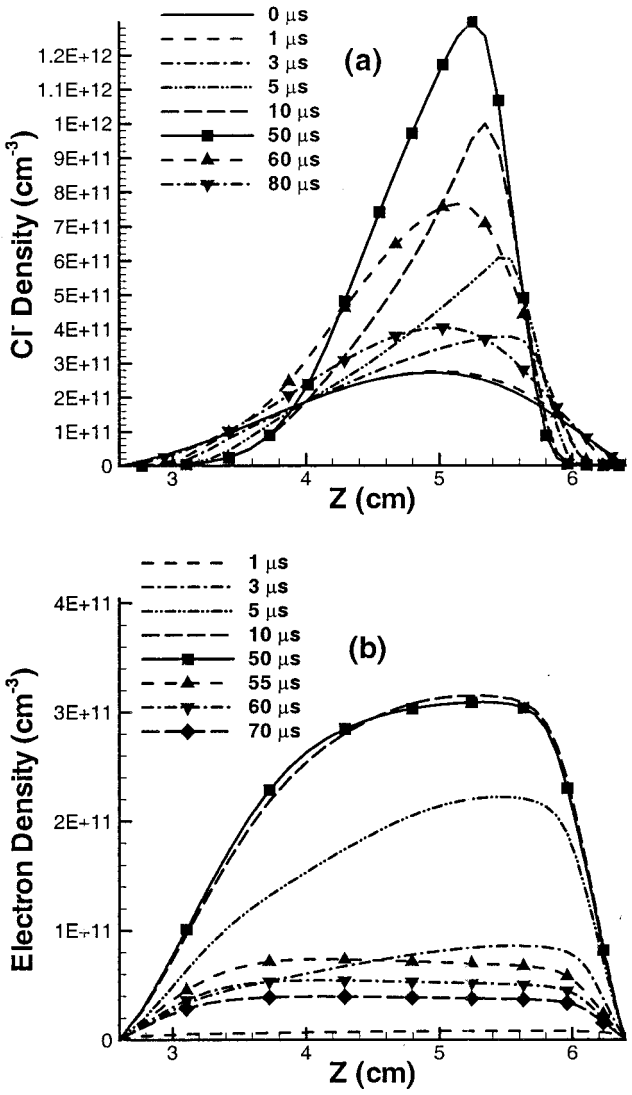

FIG. 9. Density evolution along the axial direction at a radius of 2.4 cm for (a) negative ions and (b) electrons (base case conditions, Table II).

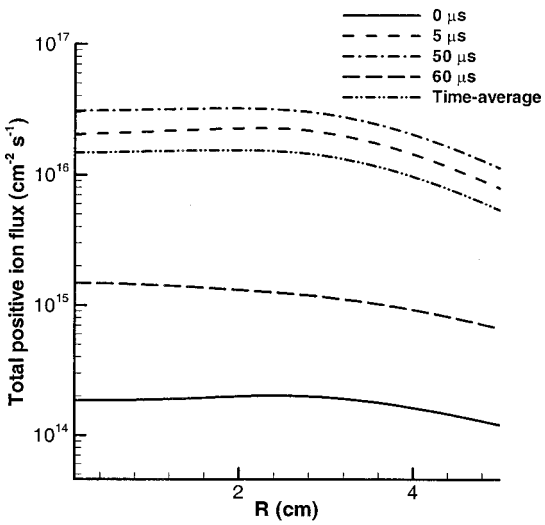

FIG. 10. Evolution of total positive ion flux on substrate electrode during a pulse (base case conditions, Table II).

Figure 7 shows the quasi-steady state profile of the Cl atom density. A peak occurs in the core of the discharge where the electron density is highest, and Cl atoms are produced mainly by dissociation of molecular chlorine (reaction R6 in Table I). Although the Cl atom production rate peaks off axis, the density itself peaks on axis due to diffusion ''filling in.'' The Cl atom density drops off near the walls due to surface recombination. The Cl atom density in the outer region of the cell is low due to a much lower rate of production of Cl (low electron density and temperature) and wall recombination. However, diffusion keeps the Cl atom density substantial even in the outer region. Since the time scale for neutral transport and reaction is of the order of a few milliseconds, the Cl atom density responds to the time averaged power deposited in the plasma, rather than the instantaneous power.

The temporal variation of the negative ion density at three axial locations in the discharge (measured from the substrate electrode, all at a radius of 2.4 cm) is shown in Fig. 8. Line (a) corresponds to 1.4 cm (closest to the substrate electrode), line (b) is for 2.6 cm (near the central plane), while line (c) is for 3.4 cm (nearest to the quartz window). Line (c) shows an initial abrupt drop in the negative ion density near the quartz window as the power is turned on, due to the formation of electrostatic fields squeezing negative ions towards the plasma [see also Figs. 6(c) and 6(d)]. The fields exists so long as the power is on; hence there are virtually no negative ions at that location for the duration of the active glow. In the afterglow, the field disintegrates allowing negative ions to back diffuse and escape to the wall, thus leading to a rise in the negative ion density [see also Fig. 9(a)]. Near the substrate electrode (line a), however, squeezing is less prominent since the ambipolar field is not strong enough to exclude negative ions from that location. Near the center of the discharge (line b), the negative ion density increases monotonically during the active glow as negative ions pile up (in part due to the squeezing referred to above) near the center. In the afterglow, the negative ion density decreases monotonically due to negative ions diffusing back towards the walls.

The line plots in Fig. 9(a) show the negative ion squeezing along the axial direction (at $R=2.4$ cm) during the active glow and the back diffusion of negative ions during the afterglow. In fact, the negative ion density profiles on the quartz window side (at z near 6 cm) show the formation of a self-sharpening front, during the active glow. The electron density along the axial direction is shown in Fig. 9(b) for various times during a pulse. The asymmetry in the electron density profile is due to the asymmetry in the power deposition. In regions where the electronegativity is high, the electron density profile tends to be uniform, as discussed earlier (Fig. 4). The formation of an ion–ion plasma occurs at $\sim 15\ \mu$s into the afterglow.

Since etch rates depend on the flux of ions impinging on the substrate electrode, the evolution of the positive and negative ion flux striking the substrate electrode was inves-

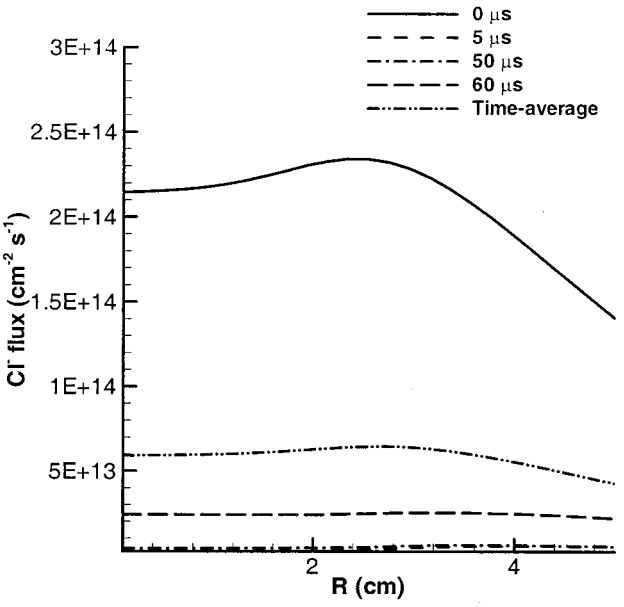

FIG. 11. Evolution of Cl^- flux on substrate electrode during a pulse (base case conditions, Table II).

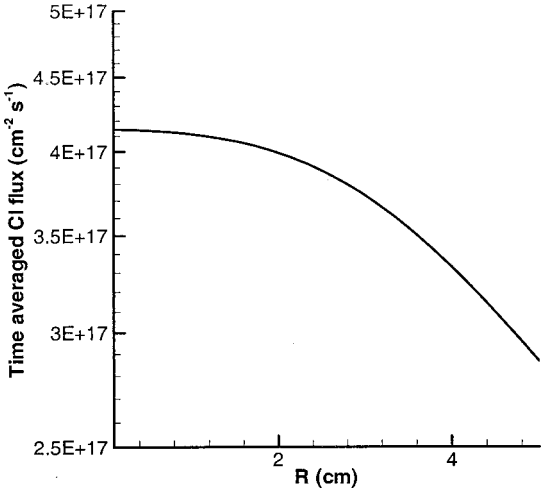

FIG. 12. Time-averaged Cl flux on substrate electrode (base case conditions, Table II).

tigated. Figure 10 shows that the total (Cl^+ and Cl_2^+) positive ion flux is quite uniform over a 3 cm radius, falling off near the edges. The positive ion flux varies by two orders of magnitude during a pulse. It is very low, limited by free diffusion, in the late afterglow when an ion–ion plasma exists. It rises during the active glow when the ion density increases and ambipolar diffusion sets in. The negative ion flux in Fig. 11 is seen to decrease rapidly in the early active glow due to the formation of electrostatic fields, squeezing negative ions inside the discharge. The negative ion flux increases in the afterglow as the field disintegrates and negative ions back diffuse towards the walls. The Cl atom flux along the substrate electrode is shown in Fig. 12. The profile is quite non-uniform as Cl atoms diffuse towards the outer region of the reactor.

Figures 11 and 12 show that the positive and negative ion fluxes differ drastically during the active glow of the discharge. In order to extract equal currents of positive and negative ions (to minimize charging damage), one would have to wait for the formation of an ion–ion plasma ($\sim$15 μs into the afterglow for the base case conditions) and then apply rf bias to perform anisotropic etching using these ions. Of course, such action reduces throughput. Reduction in throughput could be partly offset if it were possible to design a spatial afterglow reactor. Such a system would be a cw plasma in a strongly electronegative gas (e.g., SF_6) at appropriate pressure such that a steady state ion–ion plasma could form over the wafer an appropriate distance downstream of the power deposition zone.

Comparison with experimental data. Continuous wave (steady state, no pulsing) plasma simulations were performed

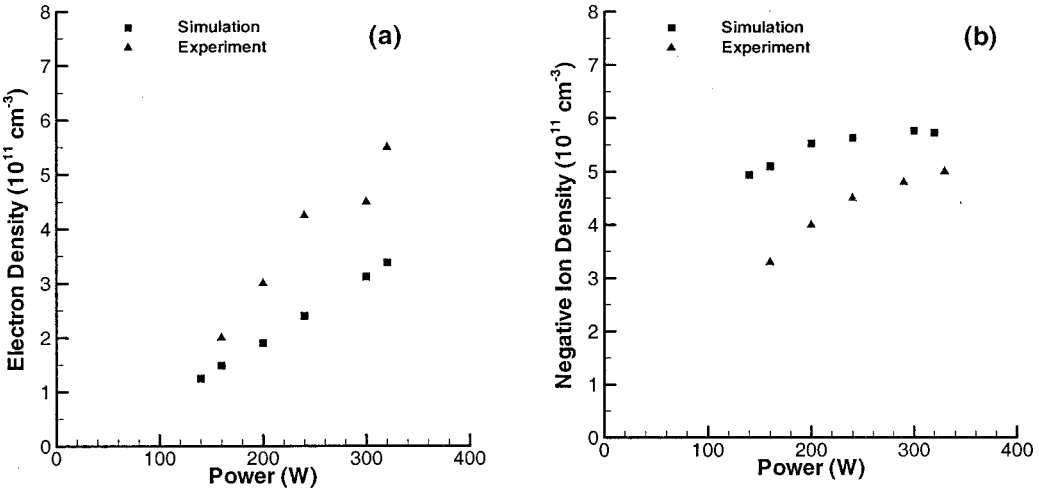

FIG. 13. Comparison between simulated (squares) and experimentally measured (Ref. 26) densities (triangles) as a function of power. (a) Electrons and (b) negative ions, for steady state plasmas.

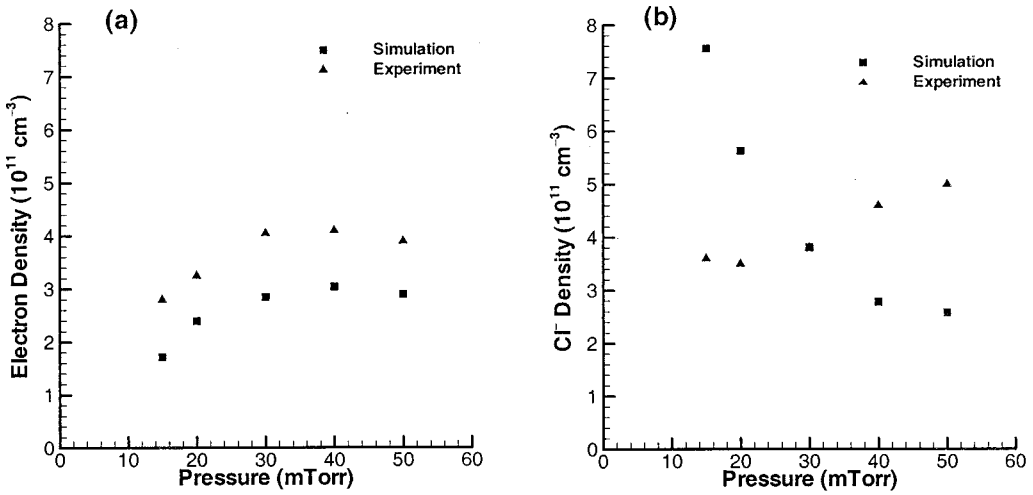

FIG. 14. Comparison between simulated (squares) and experimentally measured (Ref. 26) (triangles) densities as a function of pressure. (a) Electrons and (b) negative ions, for steady state plasmas.

at given power and pressure to facilitate comparison of simulation predictions with experimental data. The electron and negative ion densities computed (squares) at the center of the discharge ($R=0$, $z=4.5$ cm) are compared with experiments (triangles)[26] as a function of power (Fig. 13) and pressure (Fig. 14). No adjustable parameters of any kind were used in this comparison. The agreement between simulation and experiment is reasonable [except for Fig. 14(b)] in the sense that the uncertainty of the experimental values is within the range of the simulation predictions. The electron density varies linearly with power [Fig. 13(a)] and goes through a shallow maximum with pressure [Fig. 14(b)]. The negative ion density rises with power [Fig. 13(b)], although the simulation predicts a slower rise compared to experiment. However, the simulation predicts a strong decrease of negative ion density with pressure at the discharge center, while experiment shows a mild increase. This predicted behavior is due to the strong dependence of the negative ion density on position, as pressure varies [Fig. 15(a)]. The negative ion density right at the center of the discharge ($R=0$) decreases drastically with pressure. Nevertheless, the simulation predicts that both the peak and the line integrated negative ion density increase mildly with pressure [Fig. 15(b)], in accord with experiments. The negative ion density in the experiment was measured by laser photodetachment and is therefore limited by the spatial resolution of the technique. The measurement is in reality over a small volume around the discharge center, not at the center. The above discussion underscores the importance of spatial resolution in making negative ion measurements, since the negative ion density profiles can be varying strongly with position.

Further comparisons of simulation predictions with experimental data[24] were performed for pulsed plasmas by varying the duty ratio and peak power. The electron densities shown in Figs. 16 and 17 are line integrated averages, obtained by integrating the electron density radially along the

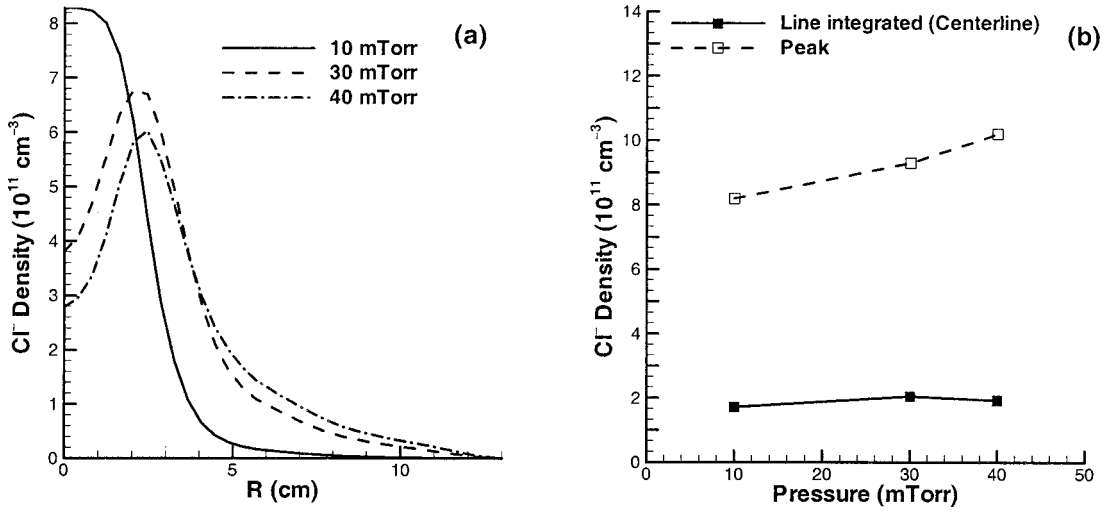

FIG. 15. (a) Radial profiles of negative ion density at the central axial plane of the discharge in steady state plasmas. (b) Peak and line integrated (radially through the discharge center) values of negative ion density for 10, 30, and 40 mTorr pressure in steady state plasmas.

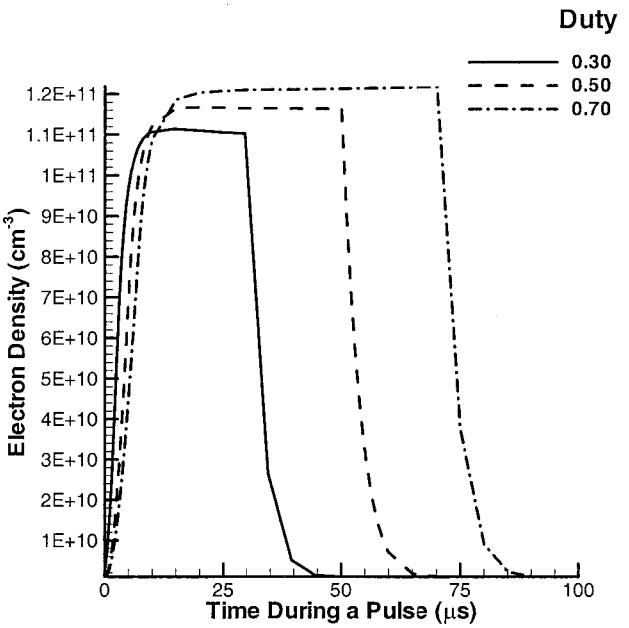

FIG. 16. Time evolution of line averaged (through the discharge center) electron density for pulsed plasmas with duty ratios of 0.3, 0.5, and 0.7 (other conditions at base case values, Table II).

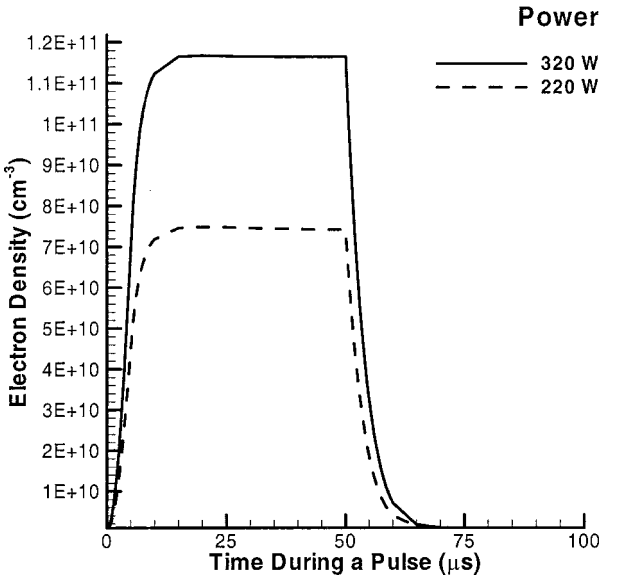

FIG. 17. Time evolution of line averaged (through the discharge center) electron density for pulsed plasmas with two different peak powers (other conditions at base case values, Table II).

centerline (at $z=4.5$ cm). Figure 16 shows a monotonic increase in the peak (plateau) electron density as the duty ratio is increased. As the duty ratio increases, the degree of molecular dissociation also increases (remember that the degree of dissociation depends on the time-average power). Since total electron energy losses per ionization event are higher for molecular than for atomic chlorine, more electrons are needed to consume the same amount of peak power as the duty ratio increases. Experiments,[24] however, indicate that the peak electron density varies nonmonotonically as the duty ratio is increased. The peak electron density initially increases with increasing duty ratio and then decreases. This discrepancy is not clear at the present time. Nevertheless, qualitative agreement between simulation and experiment is found when the peak power varies (for a constant duty ratio). The peak (plateau) electron density increases with increasing peak power in both simulation (Fig. 17) and experiment.[24]

V. CONCLUSIONS

A two-dimensional self-consistent simulation of an inductively coupled pulsed-power (square-wave modulated) chlorine plasma was developed based on the fluid approximation. The equations for the inductive power deposition were coupled to the plasma transport equations to capture the space and time evolution of the discharge. In the active glow, spontaneous separation of the plasma into an ion–ion core (with high electronegativity) and an electropositive edge was observed. Negative ions were found to be squeezed into the plasma during the active glow due to emerging electrostatic fields at the edge. This squeezing was more pronounced near the quartz window where the bulk of power deposition takes place. An initial spike in the electron temperature was observed which has also been observed experimentally. The electron temperature was found to peak in the region of power deposition under the coil. However, considerably warm temperatures were seen away from the power deposition zone due to the high thermal conductivity of the electrons. The fractional dissociation was found to be highest in the core of the discharge.

The time evolution of the negative ion density during a pulse was strongly dependent on the spatial location in the discharge. This was attributed to transport processes of negative ion squeezing during the active glow and back diffusion in the afterglow. This underscores the need to carefully control the spatial resolution of experimental probes used to measure the negative ion density. The formation of an ion–ion plasma was seen to occur at ~ 15 μs in the afterglow. By that time most of the electrons have escaped and the plasma decays by (almost) free ion diffusion to the walls.

Reasonable agreement between simulation predictions and experimental data was found for the variation of electron and negative ion densities with power and pressure in steady state plasmas. In pulsed plasmas, agreement was again found for the variation of electron density with input peak power. However, the experimental variation of electron density with duty ratio was more complex than the monotonic increase predicted by the simulations.

ACKNOWLEDGMENTS

Many thanks for the financial support by the National Science Foundation through NSF CTS-9713262 and CTS-0072854.

[1]M. A. Lieberman and A. J. Lichtenberg, *Principles of Plasma Discharges and Materials Processing* (Wiley, New York, 1994).
[2]R. Boswell and R. Porteous, J. Appl. Phys. **62**, 3123 (1987).

[3]P. Jiang, D. J. Economou, and C. B. Shin, Plasma Chem. Plasma Process. **15**, 383 (1995); S.-K. Park and D. J. Economou, J. Electrochem. Soc. **137**, 2103 (1990).
[4]J. Verdeyen, J. Bederman, and L. Overzet, J. Vac. Sci. Technol. A **8**, 1851 (1990).
[5]T. H. Ahn, K. Nakamura, and H. Sugai, Plasma Sources Sci. Technol. **5**, 139 (1996).
[6]V. Midha and D. J. Economou, Plasma Sources Sci. Technol. **9**, 256 (2000); I. Kaganovich, D. J. Economou, and B. N. Ramamurthi, Phys. Rev. E **64**, 036402 (2001).
[7]I. Kaganovich, D. J. Economou, B. N. Ramamurthi, and V. Midha, Phys. Rev. Lett. **84**, 1918 (2000).
[8]A. A. Kudryavtsev and L. D. Tsendin, Tech. Phys. Lett. **26**, 582 (2000); R. N. Franklin and J. Snell, J. Phys. D **33**, 2019 (2000).
[9]S. Kananasabapathy, L. Overzet, V. Midha, and D. J. Economou, Appl. Phys. Lett. **78**, 22 (2001).
[10]M. Meyyappan, J. Vac. Sci. Technol. A **14**, 2122 (1996).
[11]S. Ashida and M. A. Lieberman, Jpn. J. Appl. Phys., Part 1 **36**, 854 (1997).
[12]D. P. Lymberopoulos, V. I. Kolobov, and D. J. Economou, J. Vac. Sci. Technol. A **16**, 564 (1998).
[13]P. J. Hargis, K. E. Greenberg, P. A. Miller, J. B. Gerardo, J. R. Torczynski, M. E. Riley, G. A. Hebner, J. R. Roberts, J. K. Olthoff, J. R. Whetstone, J. R. Van Brunt, M. A. Sobolewski, H. M. Anderson, M. P. Schlikal, J. L. Mock, P. Bletzinger, A. Garscadden, R. A. Gottscho, G. Selwyn, M. Dalvie, J. E. Heidenreich, J. W. Butterbaugh, M. L. Brake, M. L. Passow, J. Pender, A. Lujan, M. E. Elta, D. B. Graves, H. H. Sawin, M. J. Kushner, J. T. Verdeyan, R. Horwarth, and T. R. Turner, Rev. Sci. Instrum. **65**, 140 (1994).
[14]R. Wise, D. Lymberopoulos, and D. J. Economou, Appl. Phys. Lett. **68**, 2499 (1996); R. S. Wise, D. P. Lymberopoulos, and D. J. Economou, in *Proceedings of the Eleventh Plasma Processing Symposium*, edited by G. S. Mathad, M. Meyyappan, and D. W. Hess (Electrochemical Society, New York, 1996), **PV-96-12**, p. 11; J. Economou, J. Feldsien, and R. S. Wise, in *Electron Kinetics and Applications of Glow Discharges*, edited by U. Kortshagen and L. D. Tsendin, NATO Advanced Research Workshop (Plenum, New York, 1998).
[15]D. P. Lymberopoulos and D. J. Economou, J. Res. Natl. Inst. Stand. Technol. **100**, 473 (1995).
[16]D. P. Lymberopoulos and D. J. Economou, IEEE Trans. Plasma Sci. **23**, 573 (1995).
[17]J. Helmsen, D. Hammer, J. Yamartino, and P. Loewenhardt, IEEE Trans. Plasma Sci. **27**, 58 (1999).
[18]S. S. Kim, C. S. Chang, N. S. Yoon, and K. W. Whang, Phys. Plasmas **6**, 2926 (1999).
[19]V. I. Kolobov and D. J. Economou, Plasma Sources Sci. Technol. **6**, R1 (1997).
[20]E. F. Jaeger, L. A. Berry, J. S. Tolliver, and D. B. Batchelor, Phys. Plasmas **2**, 2597 (1995).
[21]V. Midha and D. J. Economou, J. Electrochem. Soc. **144**, 4062 (1997).
[22]N. Brooks and T. J. R. Hughes, Comput. Methods Appl. Mech. Eng. **32**, 199 (1982).
[23]D. Byrne and A. C. Hindmarsh, J. Comp. Phys. **70**, 1 (1987).
[24]A. Hebner and C. B. Fleddermann, J. Appl. Phys. **82**, 2814 (1997).
[25]V. Malyshev, V. M. Donnelly, J. I. Colonell, and S. Samukawa, J. Appl. Phys. **86**, 4813 (1999).
[26]A. Hebner, J. Vac. Sci. Technol. A **14**, 2158 (1996).